Analysis of Matrix Completion Algorithms for Spectral Image Estimation from Compressive Coded Projections

Carlos Alberto Hinojosa Montero, Henry Arguello Fuentes
Universidad Industrial de Santander
carlos.hinojosa1@correo.uis.edu.co, henarfu@uis.edu.co

Hoover Rueda Chacón
Delaware University
rueda@udel.edu

Abstract

The coded aperture snapshot spectral imaging (CASSI) system is an optical architecture designed to capture spectral images using the compressive sensing (CS) concepts. CASSI senses the spectral information of a three dimensional scene by using two-dimensional coded focal plane array (FPA) projections. The CASSI system improves the sensing speed and reduce the large amount of collected data given by conventional spectral imaging systems based on the Nyquist criterion. Compressive sensing reconstruction algorithms are commonly used to recover the underlying three dimensional source. However, CS assumes the signal is sparse, which is not always achievable. This work proposes the use of Matrix Completion (MC) theory as an alternative way to reconstruct the underlying three dimensional source from the compressive coded projections. The reconstruction is accomplished by solving a convex optimization problem, which relies on the nuclear-norm minimization of the measurement, subject to data constraints. Further, it is proposed and analyzed the impact of six different linear transformations to arrange the missing data, such that the degrees of freedom of the transformed matrix ease the completion process. Simulations show good quality of the reconstruction and it is observed that MC algorithms are much faster than conventional CS reconstruction algorithms.

1. Introduction

Imaging spectroscopy (also hyperspectral or spectral imaging) involves the sensing of a large amount of spatial information across a multitude of wavelengths, making it an useful tool for applications in astronomy [1], agriculture [2], biomedical imaging [3], geosciences [4], physics, and surveillance [5]. More precisely, hyperspectral images are sets of two-dimensional images collected across the electromagnetic spectrum. These data sets are regarded as three-dimensional images, where two of their components correspond to the spatial domain and the third represents the spectral information.

Many different techniques for spectral imaging have been developed over the years. For instance, whiskbroom [6], pushbroom [7], and tunable filter [8] imagers are all conceptually simple spectral imager designs. These approaches of hyperspectral image sensing scan adjacent zones of the underlying spectral scene and merge the results to construct a spectral 3D data cube. These methods are based on the Shannon-Nyquist theory for signal acquisition, thus they require scanning a number of zones linearly in proportion to the desired spatial or spectral resolution.

A novel architecture known as the coded aperture snapshot spectral imaging (CASSI) system has been developed for the acquisition of compressive spectral image data with just a few coded focal plane array (FPA) measurements [9]. This architecture exploits the compressive sensing (CS) theory and efficiently senses a signal taking a set of random coded projections from the underlying scene. CASSI measurements are realized optically by a coded aperture, a dispersive element such as a prism, and a FPA detector [10] [11]. The CASSI projections are given by $\mathbf{g} = \mathbf{Hf}$, where $\mathbf{H}$ is an $N(N+L-1) \times (N^2 \cdot L)$ matrix determined by the coded apertures and the dispersive element used in CASSI and $\mathbf{f}$ is the input spectral database. Using the random projections, a CS reconstruction algorithm, based on ℓ_1 norm minimization, is then used to reconstruct the initial signal [12] [13]. Although this algorithms provide an accurate recovery, they are computationally expensive. Due to the CASSI system senses and compress the initial signal, the reconstruction of the scene can be modeled as a decompression process. Therefore, the main problem consist in finding the missing entries of the decompressed data cube.

This work proposes the use of Matrix Completion (MC) theory as an alternative way to reconstruct the initial signal from the compressive coded projections. It has been recently shown that most low-rank matrices can be exactly recovered from most sets of sampled entries, even though these sets have surprisingly small cardinality [14]. In essence, MC algorithms attain an estimation of the input

978-1-4673-9461-1/15/$31.00 ©2015 IEEE

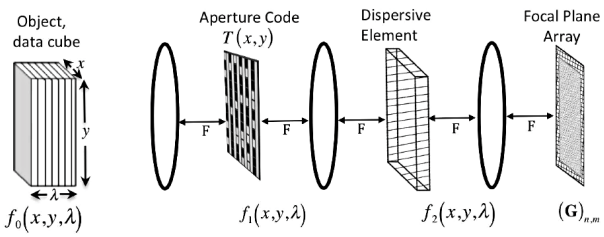

Figure 1. Optical elements present in CASSI

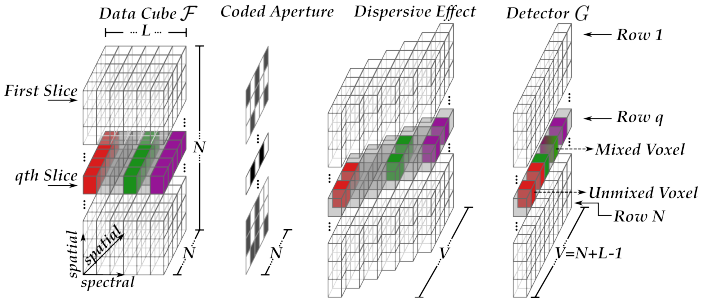

Figure 2. An illustration of the spectral optical flow in CASSI. The qth slice of the data cube $\mathcal{F}$ is coded by a row of the coded aperture and dispersed by the prism. The detector captures the intensity by integrating the coded light. This intensity can be represented as mixed and unmixed voxels.

signal by minimizing the sum of the singular values of the measurement matrix, i.e. they find a matrix with minimum nuclear norm that fits the sampled data [15], [16]. Completing a matrix from a sampling of its entries is a problem of rapidly growing interest in many areas of science and engineering including collaborative filtering [17], machine learning [18], control, remote sensing, seismic data reconstruction [19], and computer vision [20], to name a few.

For the specific case of hyperspectral matrix completion using the CASSI, note that the amount of sampled measurements ($N(N+L-1)$) is far less than the number of 3D data cube entries to be estimated (N^2L). Therefore, the problem to solve becomes extremely ill posed, because there are infinitely many completions. In this paper, it is proposed and analyzed the impact of six different linear transformations to arrange the missing data, such that the degrees of freedom of the transformed matrix ease the completion process. Several simulations were performed to compare the six proposed linear transformations, and the attained results show good quality of the reconstructions. Also it is observed that MC algorithms are much faster than conventional CS reconstruction algorithms.

2. THE CASSI SPECTRAL SENSING MODEL

The CASSI system is depicted in Fig. 1 [11]. The spatio-spectral density source $f_0(x, y, \lambda)$, where (x, y) are the spatial coordinates and λ is the wavelength, is first coded by a coded aperture $T(x, y)$ and then, the resulting coded field $f_1(x, y, \lambda)$ is spectrally dispersed by a dispersive element before it impinges on the FPA as

$$f_2(x,y,\lambda) = \int\int T(x',y') f_0(x',y',\lambda) \times h(x'-\alpha\lambda-x, y'-y)dx'dy', \quad (1)$$

where $T(x', y')$ is the transmission function representing the coded aperture, $h(x' - \alpha\lambda - x, y' - y)$ is the optical impulse response of the system, and $\alpha\lambda$ is the dispersion induced by the prism assuming a linear dispersion. Each spectral slice of the data cube is thus spatially modulated by the coded aperture and dispersed by the dispersive element [11]. The compressive measurements across the FPA are realized by the integration of the field $f_2(x, y, \lambda)$ over the detector's spectral range sensitivity.

The discrete model of the sensing mechanism is shown in Fig. 2. There, the analog spatio-spectral source $f_0(x, y, \lambda)$ is discretized as $\boldsymbol{\mathcal{F}}_{mnk}$, where m and n index the spatial coordinates, and k determines the k^{th} spectral plane. The mentioned data cube $\boldsymbol{\mathcal{F}}$ have L spectral bands and $N \times N$ spatial pixels. At the sensing process, $\boldsymbol{\mathcal{F}}$ is first amplitude modulated by a pixelated $N \times N$ *black-* and *white-* coded aperture $\boldsymbol{T}$ such that the intensity along the spectral coordinate of the data cube is blocked when a black-coded aperture element is encountered. After, when the coded source transverses the prism, it is spatially sheared along one spatial axis. Finally, the coded and dispersed field impinges on each detector element where the intensity is integrated. The discretized output at the detector is given by

$$\boldsymbol{G}_{mn} = \sum_{k=0}^{L-1} \boldsymbol{\mathcal{F}}_{m(n-k)(k)} \boldsymbol{T}_{m(n-k)} + \boldsymbol{\omega}_{mn}, \quad (2)$$

where $\boldsymbol{G}_{mn}$ is the intensity measured at the m, n position of the detector whose size is $N \times (N + L - 1)$, $\boldsymbol{T}_{mn}$ is the $N \times N$ *black-* and *white-* coded aperture, and $\boldsymbol{\omega}_{mn}$ is the noise of the system. In essence Eq. (2) sums each of the spectral image slice that have been coded and spatially shifted in proportion to the wavelength index k. Note that the $N \times N$ spatial dimensions of the spectral data cube are mapped to an array of $V \times N$ FPA measurements, where $V = N + L - 1$. This is due to the dispersion of the optical field as it transverses the prism.

For spectrally rich scenes or very detailed spatial scenes, a single-shot FPA measurement is not sufficient, and additional shots are required, each with distinct coded aperture that remains fixed during the integration time of the detector. The ensemble of say, $K \ll L$ FPA shots in one-

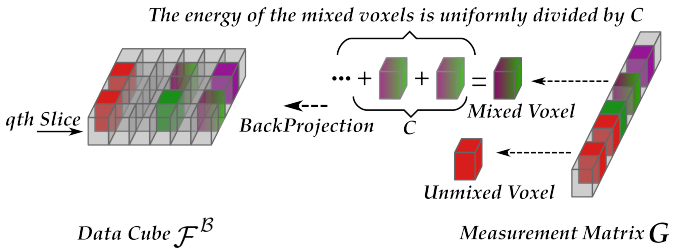

Figure 3. Backprojection Process.

dimensional vectorized form $\mathbf{g} = [\mathbf{g}_0^T, ..., \mathbf{g}_{k-1}^T]^T$, can be rewritten in the standard form of an underdetermined system of linear equations

$$\mathbf{g} = \mathbf{A}\boldsymbol{\theta} + \boldsymbol{\omega} = \mathbf{H}\boldsymbol{\Psi}\boldsymbol{\theta} + \boldsymbol{\omega}, \tag{3}$$

where $\mathbf{A} = \mathbf{H}\boldsymbol{\Psi} \in \mathbb{R}^{KVN \times N^2 L}$ is the CASSI sensing matrix, $\boldsymbol{\theta} \in \mathbb{R}^{N^2 L \times 1}$ is a sparse representation of the data cube in a three-dimensional (3-D) basis $\boldsymbol{\Psi}$, and $\boldsymbol{\omega}$ represents the noise of the system. The matrix $\mathbf{H}$ accounts for the effects of the coded aperture and the prism [21]. In this paper, the dispersive element is considered linear and the system noise is not considered. Conventionally, given the set of measurements $\mathbf{g}$, the underlying scene reconstruction process in CASSI is accomplished by using a compressive sensing algorithm which recovers $\boldsymbol{\theta}$ by solving the $\ell_2 - \ell_1$ problem

$$\arg\min_{\boldsymbol{\theta}} \|\mathbf{g} - \mathbf{A}\boldsymbol{\theta}\|^2 + \tau\|\boldsymbol{\theta}\|_1, \tag{4}$$

where τ is a regularization constant.

In contrast, the proposed method consists of recovering the underlying scene using Matrix Completion. That is, given a subset of the source matrix entries, an MC algorithm recovers the missing entries by solving a convex optimization problem. In order to use MC, the input subset data cube $\boldsymbol{\mathcal{F}}^B$ of the MC algorithm is built by backprojecting the coded compressive measurement matrix $\boldsymbol{G}$. Due to the intensity multiplexing process occurring on the FPA, $\boldsymbol{\mathcal{F}}^B$ is composed of mixed and unmixed voxels. As depicted in Fig. 2, the mixed voxels are a combination of voxels from different spectral bands which "collide" during the integration process in the CASSI i.e, mixed voxels contain information from more than one spectral band. Furthermore, unmixed voxels are voxels from a specific spectral band which do not "collide" with others voxels. More formally, let $k' \in \{0, ..., L-1\}$, the $\boldsymbol{\mathcal{F}}^B$ data cube is represented as

$$\boldsymbol{\mathcal{F}}^{\boldsymbol{\mathcal{B}}}{}_{m(n-k)k} = \begin{cases} \boldsymbol{G}_{mn}, & \boldsymbol{T}_{m(n-k)} = 1 \Leftrightarrow k = k' \\ \boldsymbol{G}_{mn}/C_{mn}, & \text{otherwise} \end{cases} \tag{5}$$

$\forall k \in \{0, ..., L-1\}$, where C_{mn} is the number of voxels being integrated in a unique $\boldsymbol{G}_{mn}$ FPA pixel. Note that the first case of Eq. (5) corresponds to the unmixed voxels and the second corresponds to the mixed voxels. The final $\boldsymbol{\mathcal{F}}^B$ data cube used to recover the underlying scene via MC will be composed of all unmixed voxels and a percentage of mixed voxels. Figure 3 shows the backprojection process, performed to create $\boldsymbol{\mathcal{F}}^B$ from the measurement matrix $\mathbf{G}$.

Due to the high compression ratio of the CASSI system, there are more mixed voxels than unmixed voxels. Therefore, the information obtained by backprojecting the data cube using only the unmixed voxels is very low, such that it is impossible to recover the underlying scene. Indeed, in order to recover a low rank matrix, the MC theory states that there must exist at least one observed entry per row and per column. In order to satisfy this MC reconstruction constraint, the amount of mixed and unmixed voxels must be incremented. The relation between the amount of mixed and unmixed voxels is given by the sampling ratio defined as,

$$R = \frac{\|\boldsymbol{f}^B\|_0}{N^2 L}, \tag{6}$$

where $\boldsymbol{f}^B \in \mathbb{R}^{N^2 L}$ is the one dimensional vectorized form of $\boldsymbol{\mathcal{F}}^B$ and $\|\cdot\|_0$ accounts for the total number of non-zero elements in a vector. Taking more CASSI shots allows to obtain different information from the original data cube since each shot is taken with a different coded aperture. However, the compression ratio of the CASSI system decreases as the number of shots increases. Therefore, the amount of unmixed voxels in $\boldsymbol{\mathcal{F}}^B$ can be increased by taking more CASSI shots. The sampling ratio can also be increased by augmenting the amount of mixed voxels, nevertheless, using more unmixed voxels than mixed voxels allows to obtain a less noisy reconstruction.

3. THE MATRIX COMPLETION MODEL

Finding the missing entries of the $\boldsymbol{\mathcal{F}}^B$ data cube can be modeled as a MC problem. The general form of the problem is:

$$\begin{aligned} &\text{minimize} \quad \text{rank}(\boldsymbol{X}) \\ &\text{subject to} \quad \boldsymbol{X}_{ij} = \boldsymbol{D}_{ij},\ (i,j) \in \Omega \end{aligned} \tag{7}$$

where $\boldsymbol{D} \in \mathbb{R}^{N \times N}$ and Ω is a subset of $[N] \times [N]$ of revealed entries of $\boldsymbol{D}$. In words, Eq. (7) looks for a matrix with the lowest rank, whose entries in the set Ω correspond to the entries of $\boldsymbol{D}$. Using a projector $\mathcal{P}_\Omega(\cdot) : \mathbb{R}^{N \times N} \rightarrow \mathbb{R}^{N \times N}$ [16], defined as

$$(\mathcal{P}_\Omega(\boldsymbol{A}))_{ij} = \begin{cases} \boldsymbol{A}_{ij}, & \text{if } (i,j) \in \Omega \\ 0, & \text{otherwise} \end{cases} \tag{8}$$

the problem in Eq. (7) can be rewritten as

$$\begin{aligned} &\text{minimize} \quad \text{rank}(\boldsymbol{X}) \\ &\text{subject to} \quad \mathcal{P}_\Omega(\boldsymbol{X}) = \mathcal{P}_\Omega(\boldsymbol{D}). \end{aligned} \tag{9}$$

However, Eq. (9) is an NP-hard problem [22] and has to be relaxed for real computations. Then, Eq. (9) can be approximated by the convex problem.

$$\begin{aligned} &\text{minimize} && \|\boldsymbol{X}\|_* \\ &\text{subject to} && \mathcal{P}_\Omega(\boldsymbol{X}) = \mathcal{P}_\Omega(\boldsymbol{D}), \end{aligned} \tag{10}$$

where $\|\boldsymbol{X}\|_*$ denotes the nuclear norm (the sum of the singular values) [15], [23], [24]. Equation (9) can also be approximated by

$$\begin{aligned} &\text{minimize} && \|\mathcal{P}_\Omega(\boldsymbol{X}) - \mathcal{P}_\Omega(\boldsymbol{D})\|_F \\ &\text{subject to} && \text{rank}(\boldsymbol{X}) \leq r. \end{aligned} \tag{11}$$

This approximation is based on an a priori knowledge of the rank r and already assumes that the revealed entries are corrupted by Gaussian noise [16].

Lots of algorithms have been proposed to solve Eqs. (10) and (11), such as linearized Bregman [25], fixed point continuation with Bregman iteration [26], etc. Extensive comparisons between MC solution approaches [27], [28], [29], [26], revealed that the LMaFit algorithm (Low-Rank Matrix Fitting) [30] is overall the fastest and most reliable method for matrix completion. We refer to [31] for these results.

To complete a matrix with MC theory, this must satisfy certain constraints, such as, every row and column of the matrix must have an observed entry [15]. In order to apply the MC theory, we propose and evaluate the following six linear transformations to rearrange the $\boldsymbol{\mathcal{F}}^B \in \mathbb{R}^{N\times N\times L}$ data cube seeking to fulfill MC constraints and improve the reconstructions quality. These methods are:

1. **Spectral-Band-Splitting**: $\boldsymbol{\mathcal{F}}^B$ is splitted in L spectral bands, $\boldsymbol{\mathcal{F}}^B_k \in \mathbb{R}^{N\times N}$, where $k = 0, ..., L-1$. All spectral bands are reconstructed separately using MC and then, the individual results are merged.

2. **Vectorized-Spectral-Band**: The L spectral bands $\boldsymbol{\mathcal{F}}^B_k \in \mathbb{R}^{N\times N}$ are vectorized as $\boldsymbol{f}^B_k \in \mathbb{R}^{N^2}$ and then placed as the columns of a $N^2 \times L$ matrix. After, a MC algorithm is applied to the created matrix and finally, the result is rearranged again in a $N \times N \times L$ data cube.

3. **Row-Slice-Splitting**: $\boldsymbol{\mathcal{F}}^B$ is splitted in N row slices $\tilde{\boldsymbol{\mathcal{F}}}^B_m \in \mathbb{R}^{L\times N}$, where $m = 0, ..., N-1$. All row slices are reconstructed separately using MC and then, the individual results are merged.

4. **Vectorized-Row-Slice**: The N row slices $\tilde{\boldsymbol{\mathcal{F}}}^B_m \in \mathbb{R}^{L\times N}$ are vectorized as $\tilde{\boldsymbol{f}}^B_m \in \mathbb{R}^{L\cdot N}$ and then placed as the columns of a $L \cdot N \times N$ matrix. After, a MC algorithm is applied to the created matrix and finally, the result is rearranged again in a $N \times N \times L$ data cube.

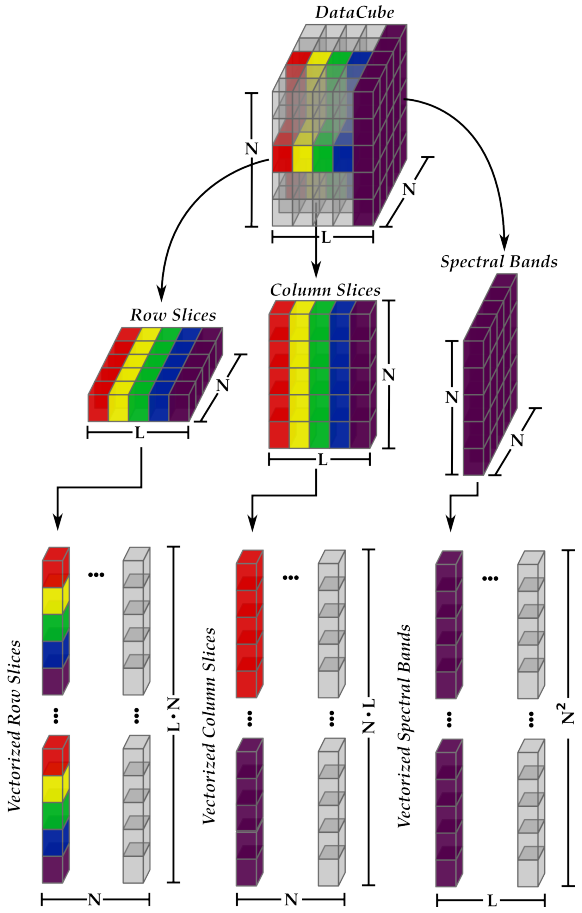

Figure 4. Linear Transformations. The data cube can be splitted in row slices, column slices and spectral bands. At the same time, each of these matrices can be vectorized and merged to form vectorized row slices, vectorized column slices and vectorized spectral bands matrices. Note the different location of each voxel through each transformation.

5. **Column-Slice-Splitting**: $\boldsymbol{\mathcal{F}}^B$ is splitted in N column slices $\hat{\boldsymbol{\mathcal{F}}}^B_n \in \mathbb{R}^{N\times L}$, where $n = 0, ..., N-1$. All column slices are reconstructed separately using MC and then, the individual results are merged.

6. **Vectorized-Column-Slice**: The N column slices $\hat{\boldsymbol{\mathcal{F}}}^B_n \in \mathbb{R}^{N\times L}$ are vectorized as $\hat{\boldsymbol{f}}^B_c \in \mathbb{R}^{N\cdot L}$ and then placed as the columns of a $N \cdot L \times N$ matrix. After, a MC algorithm is applied to the created matrix and finally, the result is rearranged again in a $N \times N \times L$ data cube.

Figure 4 depicts the proposed linear transformations that can be applied to the $\boldsymbol{\mathcal{F}}^B$ data cube in order to reconstruct the underlying scene using the MC theory.

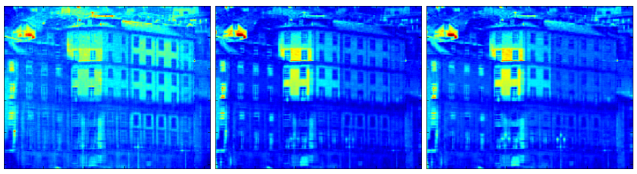

Figure 5. The 1st, 6th and 12th spectral bands of the original data cube.

4. SIMULATIONS RESULTS

A real urban scene data cube $\mathcal{F}$, with spatial resolution of 256×256 pixels and $L = 12$ spectral bands, was used to analyze the proposed MC model using the above linear transformations [32]. Figure 5 shows the 1st, 6th and 12th spectral channels of the test data cube.

The first simulation consisted in verifying if at least one nonzero entry per row and one nonzero entry per column are observed in the matrices obtained by each linear transformation, in order to satisfy the initial MC constraints for recovering the initial signal. Table 1 collects the results obtained by checking the $\mathcal{F}^{\mathcal{B}}$ data cube rearranged by the different linear transformations with all unmixed voxels and $20\%, 40\%, 60\%$ and 80% of mixed voxels, for $1, 3, 8$ and 11 CASSI shots respectively. Further, Table 2 shows the sampling ratio of the backprojected data cubes for $1, 3, 8$ and 11 shots against the different percentages of mixed voxels. As shown in Tables 1 and 2, the vectorized spectral bands, row slice splitting, and column slice splitting linear transformations can not be used for 1 CASSI shot and any percentage of mixed voxels since the low sampling ratio does not guarantee the fulfillment of the MC constraint.

The next simulations consisted in the reconstruction of the initial source data cube applying the MC algorithm. As mentioned before, the unique MC algorithm used in this simulations is LMaFit. The results were compared in terms of the peak signal-to-noise ratio (PSNR). Table 3 shows the reconstructions results for each case shown in Table 1. As shown in the Tables $1, 2$ and 3, the results can be improved by increasing the sampling ratio. This can be achieved by augmenting the number of shots and/or the percentage of mixed voxels. Nevertheless, incrementing the number of CASSI shots is better since the obtained reconstructions are less noisy due to the amount of unmixed voxels is incremented. In other words, mixed voxels aggregate noise to the backprojected data cube $\mathcal{F}^{B}$ and hence, to the reconstructions images. However, the compression ratio of the CASSI system decrease as the number of shots increase. Therefore, there is a tradeoff between taking more CASSI shots, in order to obtain a less noisy reconstruction, and taking less CASSI shots, in order to obtain a high compression ratio at the sensing process.

Figure 6 shows some images of the reconstruction results. This figure shows good estimations of the original hyperspectral data cube presented in Subfigure $6.a$. Subfigure $6.b$ presents the backprojected data cube $\mathcal{F}^{\mathcal{B}}$, with a sampling ratio of 0.6958, used for the simulations. Subfigures $6.c - 6.h$ show the reconstruction results for the Spectral-Band-Splitting, Vectorized-Spectral-Band, Row-Slice-Splitting, Vectorized-Row-Slice, Column-Slice-Splitting and Vectorized-Column-Slice linear transformations respectively. In general, the best reconstruction results were achieved by using either the Vectorized-Column-Slice or the Vectorized-Row-Slice linear transformations, obtaining 30.7265 dB and 30.7210 dB of PSNR, respectively. Also, the average time of reconstruction using LMaFit algorithm was 0.01 seconds, hence this proposed method provides fast and reliable estimations of the underlying scene.

Table 1. MC minimum observed entries constraint evaluation.

Linear Transformation	**20%**	**40%**	**60%**	**80%**
1 Shot				
Spectral-Band-Splitting	✓	✓	✓	✓
Vectorized-Spectral-Band	✗	✗	✗	✗
Row-Slice-Splitting	✗	✗	✗	✗
Vectorized-Row-Slice	✓	✓	✓	✓
Column-Slice-Splitting	✗	✗	✗	✗
Vectorized-Column-Slice	✓	✓	✓	✓
3 Shots				
Spectral-Band-Splitting	✓	✓	✓	✓
Vectorized-Spectral-Band	✗	✗	✓	✓
Row-Slice-Splitting	✗	✗	✓	✓
Vectorized-Row-Slice	✓	✓	✓	✓
Column-Slice-Splitting	✗	✗	✓	✓
Vectorized-Column-Slice	✓	✓	✓	✓
8 Shots				
Spectral-Band-Splitting	✓	✓	✓	✓
Vectorized-Spectral-Band	✗	✗	✓	✓
Row-Slice-Splitting	✗	✗	✓	✓
Vectorized-Row-Slice	✓	✓	✓	✓
Column-Slice-Splitting	✗	✗	✓	✓
Vectorized-Column-Slice	✓	✓	✓	✓
11 Shots				
Spectral-Band-Splitting	✓	✓	✓	✓
Vectorized-Spectral-Band	✗	✗	✓	✓
Row-Slice-Splitting	✗	✗	✓	✓
Vectorized-Row-Slice	✓	✓	✓	✓
Column-Slice-Splitting	✗	✗	✓	✓
Vectorized-Column-Slice	✓	✓	✓	✓

Table 2. Analysis of the sampling ratio (R) of the system.

	20%	**40%**	**60%**	**80%**
1 Shot	0.1009	0.2011	0.3002	0.3995
3 Shots	0.2140	0.4099	0.6072	0.8036
8 Shots	0.3918	0.5437	0.6958	0.8477
11 Shots	0.4868	0.6147	0.7433	0.8716

Table 3. PSNR Reconstruction Results in decibels (dB).

1 Shot				
Linear Transformation	**20%**	**40%**	**60%**	**80%**
Spectral-Band-Splitting	15.2337	17.7609	21.8450	24.6646
Vectorized-Spectral-Band	✗	✗	✗	✗
Row-Slice-Splitting	✗	✗	✗	✗
Vectorized-Row-Slice	**16.2814**	**22.3716**	24.5309	**25.0534**
Column-Slice-Splitting	✗	✗	✗	✗
Vectorized-Column-Slice	15.8778	19.6311	**24.5522**	24.9127
3 Shots				
Spectral-Band-Splitting	17.3622	23.8337	26.2400	26.5590
Vectorized-Spectral-Band	✗	✗	26.7376	26.7791
Row-Slice-Splitting	✗	✗	**26.7878**	26.8321
Vectorized-Row-Slice	**22.0313**	**26.1647**	26.6790	**26.8406**
Column-Slice-Splitting	✗	✗	26.7395	26.7794
Vectorized-Column-Slice	18.9648	26.1157	26.6098	26.7665
8 Shots				
Spectral-Band-Splitting	24.7083	28.2627	29.3270	29.3622
Vectorized-Spectral-Band	✗	✗	28.7576	28.6711
Row-Slice-Splitting	✗	✗	28.9229	28.8333
Vectorized-Row-Slice	30.2322	**31.0389**	30.7210	**30.4501**
Column-Slice-Splitting	✗	✗	29.2410	29.1054
Vectorized-Column-Slice	**31.2589**	30.6264	**30.7265**	30.4180
11 Shots				
Spectral-Band-Splitting	30.0153	30.5562	30.6954	30.5326
Vectorized-Spectral-Band	✗	✗	29.5481	29.4037
Row-Slice-Splitting	✗	✗	29.7703	29.6113
Vectorized-Row-Slice	34.1704	33.1781	32.4893	32.0309
Column-Slice-Splitting	✗	✗	30.2408	30.0206
Vectorized-Column-Slice	**34.2443**	**33.2419**	**32.5390**	**32.0389**

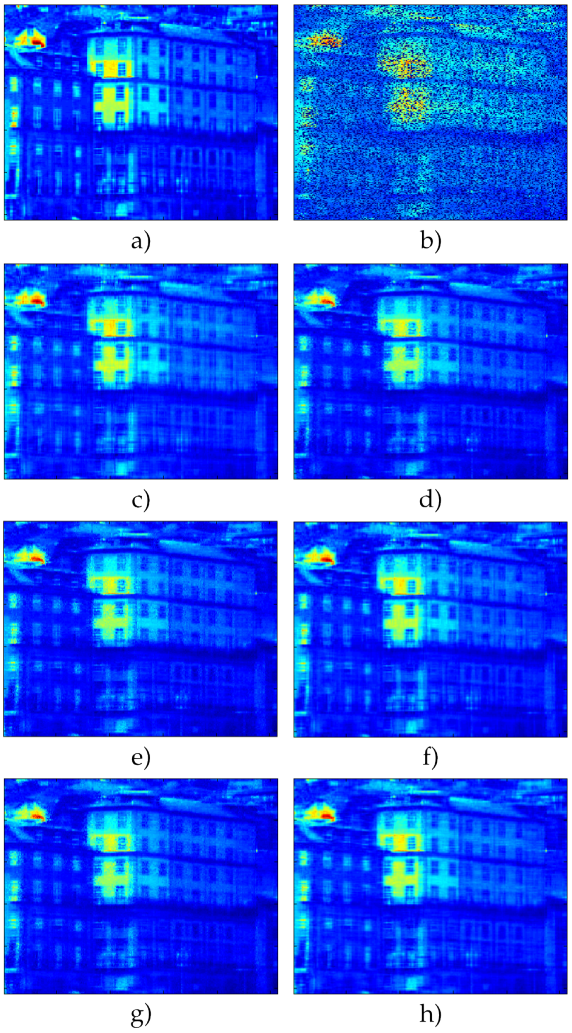

Figure 6. Reconstructions of the initial data cube using MC with the proposed linear transformations. The seventh spectral band of the original hyperspectral image is shown in a). Subfigure b depicts the seventh spectral band of the backprojected data cube $\boldsymbol{\mathcal{F}^{\mathcal{B}}}$ with sampling ratio of 0.6958. Subfigures $c) - h)$ presents the reconstruction results for the Spectral-Band-Splitting, Vectorized-Spectral-Band, Row-Slice-Splitting, Vectorized-Row-Slice, Column-Slice-Splitting and Vectorized-Column-Slice linear transformations, respectively.

5. Conclusions

In this paper it was proposed the use of the MC theory to achieve good spectral image estimations from compressive measurements using the CASSI system. Additionally, there were proposed six linear transformations to rearrange the data cube as a way to improve the estimations. The first step to setup the proposed model was to take the backprojection of the compressive coded projections of the underlying scene and creating a sample matrix as a combination of mixed and unmixed voxels. Then, the created matrix was rearranged using the six linear transformations. Finally the reconstruction was accomplished by a nuclear norm minimization algorithm. Although the results are noisy, due to the presence of mixed voxels, the matrix completion algorithm provides good reconstructions in terms of PSNR. Also, the used matrix completion algorithm is faster than any compressive sensing algorithm, therefore this approach provides a fast and reliable estimation for hyperspectral data recovery.

References

[1] R. P. Lin, B. R. Dennis, G. Hurford, D. Smith, A. Zehnder, P. Harvey, D. Curtis, D. Pankow, P. Turin, M. Bester, *et al.*, *The Reuven Ramaty high-energy solar spectroscopic imager (RHESSI)*. Springer, 2003.

[2] A. K. Tilling, G. J. OLeary, J. G. Ferwerda, S. D. Jones, G. J. Fitzgerald, D. Rodriguez, and R. Belford, "Remote sensing of nitrogen and water stress in wheat," *Field Crops Research*, vol. 104, no. 1, pp. 77–85, 2007.

[3] G. Lu and B. Fei, "Medical hyperspectral imaging: a review,"

Journal of biomedical optics, vol. 19, no. 1, pp. 010901–010901, 2014.

[4] F. Lacar, M. Lewis, and I. Grierson, "Use of hyperspectral imagery for mapping grape varieties in the barossa valley, south australia," in *Geoscience and Remote Sensing Symposium, 2001. IGARSS'01. IEEE 2001 International*, vol. 6, pp. 2875–2877, IEEE, 2001.

[5] P. W. Yuen and M. Richardson, "An introduction to hyperspectral imaging and its application for security, surveillance and target acquisition," *The Imaging Science Journal*, vol. 58, no. 5, pp. 241–253, 2010.

[6] R. O. Green, M. L. Eastwood, C. M. Sarture, T. G. Chrien, M. Aronsson, B. J. Chippendale, J. A. Faust, B. E. Pavri, C. J. Chovit, M. Solis, *et al.*, "Imaging spectroscopy and the airborne visible/infrared imaging spectrometer (aviris)," *Remote Sensing of Environment*, vol. 65, no. 3, pp. 227–248, 1998.

[7] E. Herrala, J. T. Okkonen, T. S. Hyvarinen, M. Aikio, and J. Lammasniemi, "Imaging spectrometer for process industry applications," in *Optics for Productivity in Manufacturing*, pp. 33–40, International Society for Optics and Photonics, 1994.

[8] H. R. Morris, C. C. Hoyt, and P. J. Treado, "Imaging spectrometers for fluorescence and raman microscopy: acousto-optic and liquid crystal tunable filters," *Applied spectroscopy*, vol. 48, no. 7, pp. 857–866, 1994.

[9] D. Kittle, K. Choi, A. Wagadarikar, and D. J. Brady, "Multiframe image estimation for coded aperture snapshot spectral imagers," *Applied Optics*, vol. 49, no. 36, pp. 6824–6833, 2010.

[10] D. J. Brady, *Optical imaging and spectroscopy*. John Wiley & Sons, 2009.

[11] A. Wagadarikar, R. John, R. Willett, and D. Brady, "Single disperser design for coded aperture snapshot spectral imaging," *Applied optics*, vol. 47, no. 10, pp. B44–B51, 2008.

[12] E. J. Candes, J. K. Romberg, and T. Tao, "Stable signal recovery from incomplete and inaccurate measurements," *Communications on pure and applied mathematics*, vol. 59, no. 8, pp. 1207–1223, 2006.

[13] M. A. Figueiredo, R. D. Nowak, and S. J. Wright, "Gradient projection for sparse reconstruction: Application to compressed sensing and other inverse problems," *IEEE Journal of Selected Topics in Signal Processing*, vol. 1, no. 4, pp. 586–597, 2007.

[14] R. H. Keshavan, A. Montanari, and S. Oh, "Matrix completion from a few entries," *IEEE Transactions on Information Theory*, vol. 56, no. 6, pp. 2980–2998, 2010.

[15] E. J. Candès and B. Recht, "Exact matrix completion via convex optimization," *Foundations of Computational mathematics*, vol. 9, no. 6, pp. 717–772, 2009.

[16] E. J. Candes and Y. Plan, "Matrix completion with noise," *Proceedings of the IEEE*, vol. 98, no. 6, pp. 925–936, 2010.

[17] D. Goldberg, D. Nichols, B. M. Oki, and D. Terry, "Using collaborative filtering to weave an information tapestry," *Communications of the ACM*, vol. 35, no. 12, pp. 61–70, 1992.

[18] A. Evgeniou and M. Pontil, "Multi-task feature learning," *Advances in neural information processing systems*, vol. 19, p. 41, 2007.

[19] Y. Yang, J. Ma, and S. Osher, "Seismic data reconstruction via matrix completion," *UCLA CAM Report*, pp. 12–14, 2012.

[20] C. Tomasi and T. Kanade, "Shape and motion from image streams under orthography: a factorization method," *International Journal of Computer Vision*, vol. 9, no. 2, pp. 137–154, 1992.

[21] G. R. Arce, D. J. Brady, L. Carin, H. Arguello, and D. S. Kittle, "Compressive coded aperture spectral imaging: An introduction," *IEEE Signal Processing Magazine*, vol. 31, no. 1, pp. 105–115, 2014.

[22] A. L. Chistov and D. Y. Grigor'ev, "Complexity of quantifier elimination in the theory of algebraically closed fields," in *Mathematical Foundations of Computer Science 1984*, pp. 17–31, Springer, 1984.

[23] E. J. Candès and T. Tao, "The power of convex relaxation: Near-optimal matrix completion," *IEEE Transactions on Information Theory*, vol. 56, no. 5, pp. 2053–2080, 2010.

[24] M. Fazel, *Matrix rank minimization with applications*. PhD thesis, PhD thesis, Stanford University, 2002.

[25] W. Yin, S. Osher, D. Goldfarb, and J. Darbon, "Bregman iterative algorithms for ℓ_1-minimization with applications to compressed sensing," *SIAM Journal on Imaging Sciences*, vol. 1, no. 1, pp. 143–168, 2008.

[26] S. Ma, D. Goldfarb, and L. Chen, "Fixed point and bregman iterative methods for matrix rank minimization," *Mathematical Programming*, vol. 128, no. 1-2, pp. 321–353, 2011.

[27] J.-F. Cai, E. J. Candès, and Z. Shen, "A singular value thresholding algorithm for matrix completion," *SIAM Journal on Optimization*, vol. 20, no. 4, pp. 1956–1982, 2010.

[28] Z. Lin, M. Chen, and Y. Ma, "The augmented lagrange multiplier method for exact recovery of corrupted low-rank matrices," *arXiv preprint arXiv:1009.5055*, 2010.

[29] Y.-J. Liu, D. Sun, and K.-C. Toh, "An implementable proximal point algorithmic framework for nuclear norm minimization," *Mathematical programming*, vol. 133, no. 1-2, pp. 399–436, 2012.

[30] Z. Wen, W. Yin, and Y. Zhang, "Solving a low-rank factorization model for matrix completion by a nonlinear successive over-relaxation algorithm," *Mathematical Programming Computation*, vol. 4, no. 4, pp. 333–361, 2012.

[31] M. Michenková, "Numerical algorithms for low-rank matrix completion problems," 2011.

[32] D. Foster, F. Nascimento, K. Amano, and M. Foster, "Hyperspectral images of natural scenes." `http://personalpages.manchester.ac.uk/staff/david.foster/Hyperspectral_images_of_natural_scenes_04.html`, 2004.